

Long-term replenishment strategy of SiC-doped Mn-Fe particles for high-temperature thermochemical energy storage

Di Gan^{a,b,1}, Hongbin Sheng^{a,b,1}, PeiWang Zhu^{a,b,c}, Haoran Xu^{a,b,c}, Gang Xiao^{a,b,c,*}

^a Key Laboratory of Clean Energy and Carbon Neutrality of Zhejiang Province, Zhejiang University, 38 Zheda Road, Hangzhou, Zhejiang 310027, China

^b State Key Laboratory of Clean Energy Utilization, Zhejiang University, 38 Zheda Road, Hangzhou, 310027, China

^c Jiaxing Research Institute, Zhejiang University, 1300 Dongshengxilu Road, Jiaxing, 314031, China

ARTICLE INFO

Keywords:

Replenishment model
Thermochemical energy storage
Long-term cycling
Strengthened particle
CSP plants

ABSTRACT

Thermal chemical energy storage (TCES) is a promising technology for large-scale energy storage, but long-term use of TCES materials can lead to attrition and reaction performance deterioration, compromising heat storage capacity and system continuity. To tackle this challenge, it is imperative to develop effective replenishment strategies and investigate the evolution of TCES materials. In this study, SiC-doped Mn-Fe particles exhibited superior performance, with only 1.87% mass loss ratio after 4.32×10^5 rotations attrition testing and a reaction conversion of 91.7% even after 800 reaction cycles. However, assessing material suitability for TCES systems necessitates analyzing both attrition resistance and reaction performance. A replenishment strategy was proposed, based on the attrition conversion factor and analysis of dissipated energy of particles in concentrated solar power (CSP) plants. Compared to undoped Mn-Fe particles, the annual replenishment ratio was reduced by one order of magnitude for SiC-doped particles, to only 1.26% (0.5 wt% SiC) and 0.994% (1 wt% SiC). The replenishment strategy and strengthened particles result in curtailed particle fines and particle flow interruption, and enhanced economics. Continuous replenishment strategy can undoubtedly cater to the requisite heat storage capacity demands for protracted system operation and extend system stability, promoting the advancement of TCES technology.

1. Introduction

Renewable energy sources are plagued by intermittency and variability issues, underlining the critical importance of large-scale energy storage. Thermochemical energy storage (TCES) offers advantages such as high energy storage density and long-term heat retention, making it a promising candidate for effective large-scale energy storage [35,42]. Iron-doped manganese oxides have been widely studied for thermal energy storage due to their fast reaction kinetics, low cost, non-toxicity, high reaction temperature range, high reaction conversion ratio and reoxidation ratio, high heat storage density (797.3 kJ/kg, including 595.74 kJ/kg sensible heat and 201.56 kJ/kg thermochemical heat) [49] compared to molten salt (304 kJ/kg) [14] and the use of air as a medium [3,13,46,48,49]. These advantages enable high-density thermal storage, which can further improve economic performance. However, continuous operation of the system places high demands on the long-

term characteristics of the thermal storage material and long-term operation strategy [16,21,27,42].

In CSP plants, particle fines accumulation can greatly hinder particle flow and cause reduced flowability, compromising heat storage capacity and system continuity. Recent literature highlighted the impact of mechanical strength in Mn-Fe particles on continuous operation [22,47]. Strengthening the toughness of these particles is crucial [28]. To address this issue, ongoing research has explored various approaches to enhance the mechanical strength. Agrafiotis et al. coated porous foam with $(\text{Mn}_{0.8}\text{Fe}_{0.2})_2\text{O}_3$, demonstrating reproducible performance while maintaining structural integrity after 33 cycles [2]. Azimi et al. tested several supports to enhance the attrition resistance of $(\text{Mn}_{0.75}\text{Fe}_{0.25})_2\text{O}_3$ particles [6,7]. Presiner et al. investigated the chemical stability and mechanical strength of $(\text{Mn}_{0.7}\text{Fe}_{0.3})_2\text{O}_3$ particles doped with TiO_2 , ZrO_2 , or CeO_2 and found that ZrO_2 and CeO_2 increased attrition resistance [39]. Bielsa et al. enhanced the chemical and mechanical stability of Si-doped manganese oxide particles through granulation technique optimization,

* Corresponding author at: Key Laboratory of Clean Energy and Carbon Neutrality of Zhejiang Province, Zhejiang University, 38 Zheda Road, Hangzhou, Zhejiang 310027, China.

E-mail address: xiaogantianmen@zju.edu.cn (G. Xiao).

¹ The two authors have the same contribution to this study.

<https://doi.org/10.1016/j.solener.2023.111842>

Received 25 April 2023; Received in revised form 29 June 2023; Accepted 2 July 2023

Available online 14 July 2023

0038-092X/© 2023 International Solar Energy Society. Published by Elsevier Ltd. All rights reserved.

Nomenclature*Latin letters*

E	dissipated energy
H	heat storage capacity
H_0	initial heat storage capacity
H_f	hardness
H_{remain}	remaining heat storage capacity of particles
K_f	probability of the micro protrusions on the surface will be sheared off
k_H	heat storage replenishment ratio
k_{imp}	proportionality factor of impact attrition
k_m	replenishment mass ratio
$k_{rep,annu}$	average annual replenishment rates
$k_{sum,m}$	total replenishment mass ratio
K_c	attrition volume per unit of dissipated energy
K_{fric}	frictional attrition volume loss coefficient
K_{ft}	fracture toughness
K_{imp}	impacted attrition volume loss coefficient
l	linear particle size
L	the relative sliding distance
m	mass
m_0	initial particle mass of CSP plants
n_t	number of times of replenishment
n_{year}	operation year
N	the normal force
R	attrition conversion factor
V	attrition volume loss

Greek letters

α_h	remaining heat storage capacity ratio
α_m	remaining mass ratio
θ_N	angle between force and normal direction
ρ	mass density
v_{imp}	normal velocity

Abbreviations

AR	attrition rate
CAM28	CaAl _{0.2} Mn _{0.8} O ₃₋₅
CSP	concentrated solar power
DSC	differential scanning calorimetry
Fe67	particles composed of iron–manganese oxide with a molar ratio of Fe/Mn 2:1
IR	infrared irradiation
MR	mass ratio
PRR	particle replenishment rate
sCO ₂	supercritical carbon dioxide
TRMR	total replenishment mass ratio
TCES	thermal chemical energy storage
TGA	thermal gravimetric analyzer

Subscripts

<i>cyl</i>	cylindrical drum test apparatus
<i>fric</i>	frictional attrition
<i>imp</i>	impacted attrition
<i>SH</i>	sensible heat
<i>N</i>	normal
<i>oxd</i>	oxidation reaction
<i>TCE</i>	thermochemical heat

achieving complete re-oxidation over 100 cycles and 30% increase in mechanical strength [10]. Due to excellent resistance to high temperatures, high strength, thermal stability, and low cost (compared to CeO₂ and ZrO₂ which has been proved as potential additives to increase in resistance towards attrition) [39] of SiC, some researchers use it as potential materials to increase TCES materials strength at high-temperature. Peterson et al. developed strengthened Cu-based oxygen carriers by incorporating β -SiC and calcining them to form a protective SiO₂ layer, with the porous and high-surface-area SiC structure showing potential for gas–solid reactions and particle strengthening [36]. Guo et al. improved heat transfer efficiency and mechanical stability by adapting ceramic honeycomb SiC-DPF as a side shell for CaCO₃ pellets, which was able to support a load of 1.3 MPa after 22 cycles [20]. Li et al. investigated the synergistic effects of Mn and SiC doping on the mechanical, optical, and thermal properties of CaO-based materials, and found that SiC positively impacted the crushing strength of the pellets, increasing it from 6.2 to 7.0 N after 10 cycles [30]. SiC has emerged as a promising candidate for particle mechanical strength improvement.

Besides, numerous investigations have been conducted to investigate cycling performance of manganese oxides. Wang et al. discovered that manganese-iron oxides exhibited well-preserved reduction performance after 500 cycles [40]. Carrio et al. conducted a longevity test on iron-doped manganese oxides over 75 redox cycles, demonstrating their potential for long-term cycling without deactivation [15]. Wokon et al. assessed the performance of technical grade raw material made manganese-iron binary oxide over 100 cycles in air, proving good cycling performance despite exhibiting a “swelling effect” during long-term cycles [46]. Wang et al. found that doping TiO₂ to manganese oxide resulted in better reaction performance but some agglomeration occurred [44], and Schrader et al. observed agglomeration formations of CAM28 (CaAl_{0.2}Mn_{0.8}O₃₋₅) in granular flow channels [41]. Moya et al. successfully obtained coral-like morphology by doping manganese oxide

with molybdenum, which presented excellent reaction performance after 45 cycles [34]. Bielsa et al. evaluated the synergistic effect of Si element and sol–gel method on redox performance of manganese oxides, providing complete reversibility after 40 cycles but some particle size increase [11]. Yilmaz et al. found cyclic stability and reaction performance of Mn-Si oxides improved with increasing silica content [52]. Hamidi et al. emphasized the importance of TCES material durability and cycling stability for practical application at scale when conducting reduction experiments of Fe67 (particles composed of iron–manganese oxide with a molar ratio of Fe/Mn 2:1) particles in a fixed-bed reactor using an infrared irradiation (IR) furnace [21]. Abad et al. found 1.4 wt % TiO₂-doped manganese oxides had the best oxygen uncoupling capability among all other TiO₂-doped sample, while iron oxides decreased mechanical strength [1].

However, establishing an accurate relationship between particle strength and operational performance cannot rely solely on mechanical tests. This is particularly critical for Mn-Fe particles. In CSP plants, the filling of small particles into void spaces can lead to close packing, resulting in reduced flowability [45]. Elevated temperatures increase static sliding friction, exacerbating flowability degradation [8,51]. Techno-economic analyses reveal that thermochemical particles account for 4%-12% of the total system cost of CSP plants [9,12,19,23]. Considering the additional costs resulting from severe attrition [31], it is urgent to investigate the reaction performance and attrition characteristics of Mn-Fe particles during long-term operation, establish correlations between particle attenuation process and systems operation, and provide vital data support for the design and regulation of CSP plants.

To address the aforementioned requirements, this study investigates the long-term performance evolution of SiC-doped Mn-Fe particles and their effects on CSP plants. The investigation focuses on long-term replenishment strategy based on Mn-Fe particles' attrition characteristics and reaction cycling performance, to gain insight into the effect of

particles' long-term evolution process on operation of CSP plant. Based on the models of attrition conversion factor, this study proposes a replenishment strategy for long-term system operation, providing valuable guidance for CSP plant optimizing. Optimizing particle replenishment rates [19] underscores the contribution of particle strengthening towards inventory cost reduction and improved system economics. Furthermore, identifying long-term attrition characteristics and reaction performance evolution provides crucial data support for system regulation, enabling continuous and stable CSP plant operation over the long term while promoting the development of thermochemical energy storage technology (see Fig. 1).

2. Material preparation and method

2.1. Preparation of SiC-doped Mn-Fe particles

In selecting strengthening materials for particle systems, it is crucial to ensure that they possess high-temperature stability, good thermochemical compatibility, and cost-effectiveness [32]. SiC has emerged as a promising candidate due to its excellent resistance to high temperatures, high strength, thermal stability and low cost. Therefore, SiC was selected as the doping material in this study.

SiC-doped $(\text{Mn}_{0.8}\text{Fe}_{0.2})_2\text{O}_3$ particles were synthesized using a high-temperature solid-state reaction method [43] that involved several steps, including powder mixing, extrusion, spheronization, drying, and high-temperature treatment of Mn_3O_4 (>97 wt%, Macklin), Fe_2O_3 (>99 wt%, Macklin), and SiC (>99 wt%, Macklin) powders (see Fig. 2). The molar ratios of Mn and Fe were set at 4:1 to prepare mixed oxides with 8 wt% microcrystalline cellulose (>97 wt%, Yuanye). The addition of microcrystalline cellulose is not only beneficial for the subsequent smooth extrusion of the mixed powder, but also helps to form pores inside the particles, facilitating the reaction [30]. The mixed powder was put into a drum-type ball mill and mixed for 4 h at a rotation speed of 300 r/min to ensure thorough mixing. 18 wt% of deionized water was added to the mixed powder to fully wet it for subsequent extrusion. Since the metal oxides mixed powder was relatively hard, a planetary extruder with a large torque was used for the extrusion step, and the pore size of the extrusion screen was set at 0.7 mm. The mixed powder was continuously extruded at 10 r/min to obtain a columnar object material. The extruded columnar object material was put into a centrifugal spheronizer with a rotation speed of 300 r/min for 5 min. The resulting wet particles was soft and prone to sticking together, but most of the moisture could be removed by drying at 150 °C for 1 h to reduce adhesion and facilitate high-temperature treatment to obtain dispersed particles. The dried particles were subject to high-temperature

treatment, where they were heated from room temperature to 1000 °C and kept at that temperature for 8 h to ensure full synthesizing. Afterwards, they were cooled naturally down to room temperature.

In this study, undoped $(\text{Mn}_{0.8}\text{Fe}_{0.2})_2\text{O}_3$ particles and three types of SiC-doped with doping ratios of 0.5 wt%, 1 wt%, and 5 wt% were synthesized. Properties of all four particle types were characterized through long-term tests, providing essential insights into their performance and enabling a comprehensive comparison of the effects of different doping ratio.

2.2. Long-term attrition characteristic test

To measure particle attrition characteristics during long-term operation, a cylindrical drum attrition characteristic test apparatus was designed (ASTM D4058-96). The device emulates the particle attrition process as large numbers of particles continuously impact the inner walls while being impelled by an internal baffle. The cylinders are made of wear-resistant 316 stainless steel and have an overall length of 152 mm, an inner wall diameter of 254 mm, an average wall thickness of 6 mm, and a baffle height of 51 mm (see Fig. 3). During testing, the cylinders are rotated at a constant rate of 60 r/min for a certain time, using 400 g of particles to better match actual operating conditions in the system. Before and after the attrition characteristic test, the particles are sieved and weighed, using a 50-mesh sieve for separation. All data acquisition occurs under standard ambient humidity and temperature conditions. Supporting Information provides a detailed description of the calculation of attrition ratio and attrition rate of particles.

Moreover, the particle size of the initial samples and the samples subjected to attrition characteristic test (without sieving) was analyzed using a LS-13-320-XR particle size analyzer (BECKMAN COULTER). The elemental distribution of particles was analyzed using a scanning electron microscope combined with an energy-dispersive spectrometer (SEM-EDS).

2.3. Long-term reaction performance test

Long-term reaction performance test was conducted in a muffle furnace to analyze reaction performance evolution of oxidation–reduction cycles (800 cycles) of SiC-doped $(\text{Mn}_{0.8}\text{Fe}_{0.2})_2\text{O}_3$ particles. During the reaction performance test, the particles were exposed to an ambient air atmosphere, which is consistent with the actual situation in CSP. Each cycle includes a heating segment and a cooling segment, with temperature settings at 600 oC - 1100 oC - 600 oC, corresponding to heat absorption and release processes of particles in CSP system, respectively [12]. Besides, considering the temperature difference

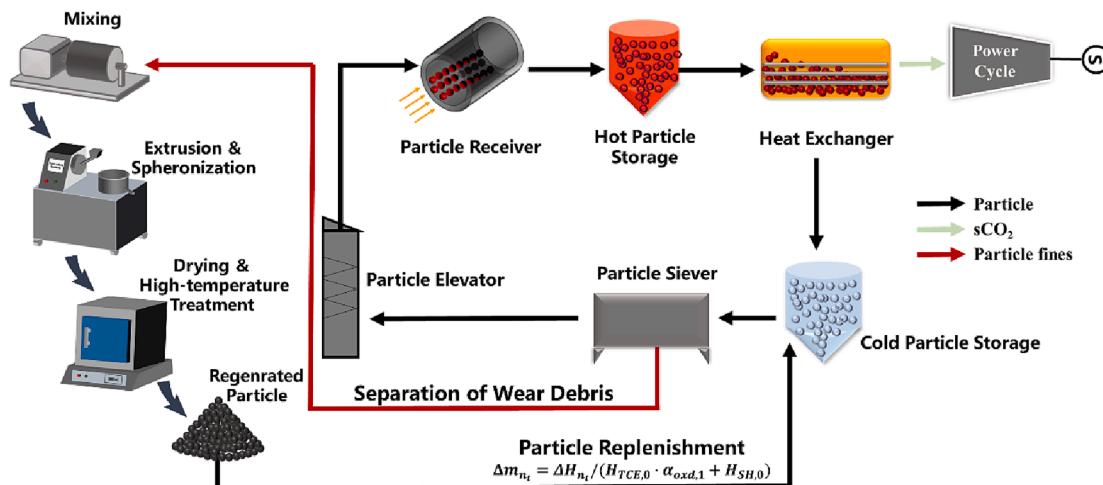


Fig. 1. Schematic diagram of the implementation of strengthen Mn-Fe particles in the CSP system.

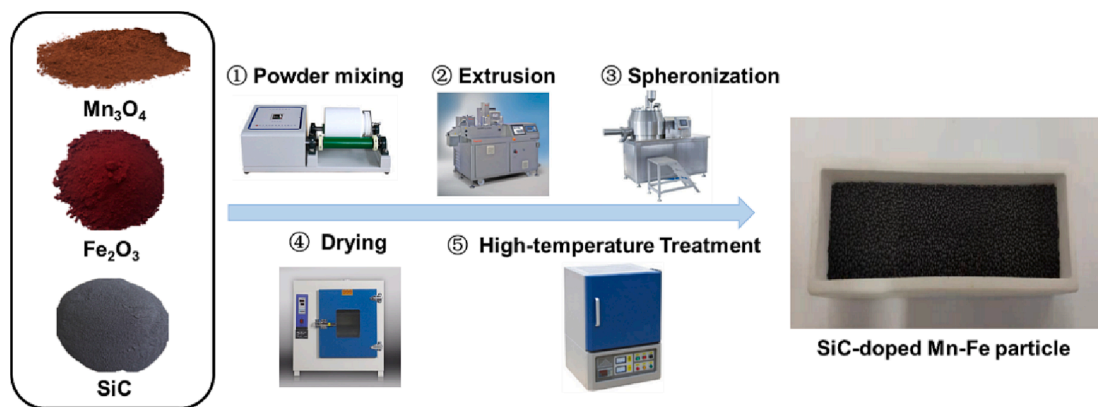


Fig. 2. Schematic diagram of the main granulation steps for $(\text{Mn}_{0.8}\text{Fe}_{0.2})_2\text{O}_3$ particles.

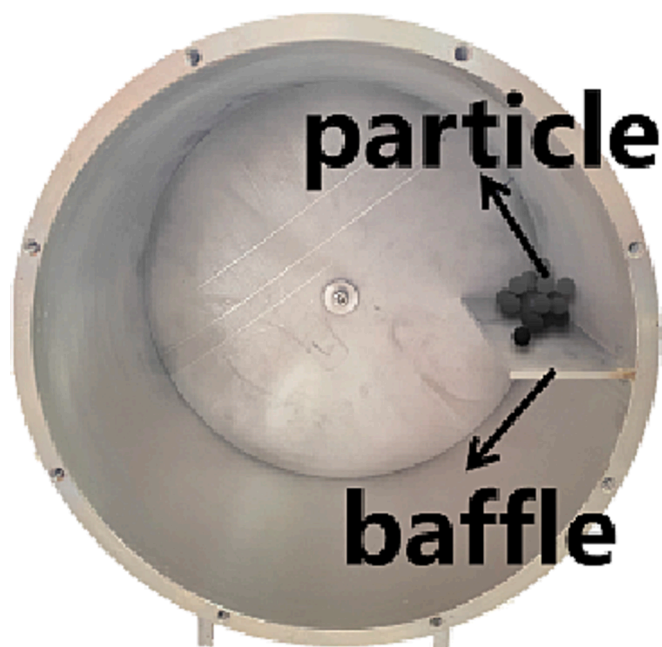


Fig. 3. Cylindrical drum attrition characteristic test apparatus.

between the set temperature during the cooling process in the muffle furnaces and the actual sample temperature, lowering the temperature to 600 °C ensures complete oxidation reaction. Long-term redox cycles were carried out to obtain samples for reaction performance degradation analysis, and a simultaneous thermal analyzer (TGA/DSC 3+, METTER TOLEDO) was used to test the reduction and oxidation performance of strengthen particles after different cycles at air atmosphere with a 50 mL min⁻¹ gas flow rate, providing a data basis for quantifying reaction performance degradation. The calculation of reduction and oxidation conversion are shown in Supporting Information. The XRD analysis was performed with a PANalytical B.V. (Netherlands) X-pert Powder diffractometer (Cu K α radiation) in the diffraction angle (2 θ) range of 10–80° with a step of 0.02° and 30 s counting time per angle. The crystal phases were identified by using the ICDD PDF-4 database

3. Characteristics analysis of particle preparation process

3.1. Analysis of water content

The water content is measured by comparing the mass changes before and after drying for 4 h at 150 °C, as shown in Fig. 4. The water content was measured for mixed powder (wet), columnar objects, wet

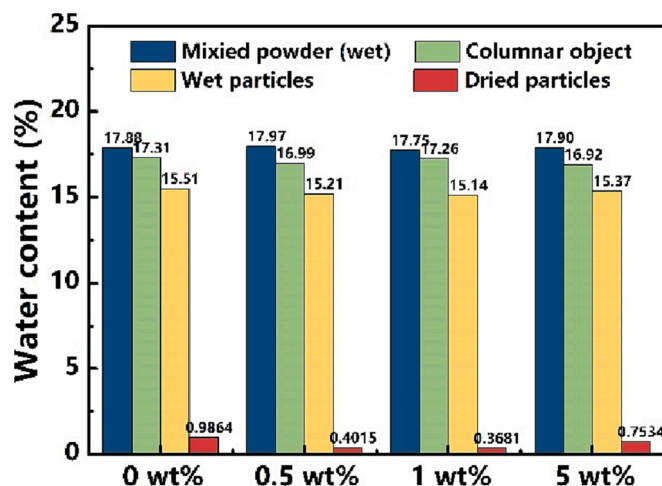


Fig. 4. Water content of different SiC-doped materials.

particles, and dried particles. It can be seen that the initial particle water content is about 18%, which gradually decreases during the granulation process. The main dehydration process occurs during drying, and the particle water content drops to <1% after drying.

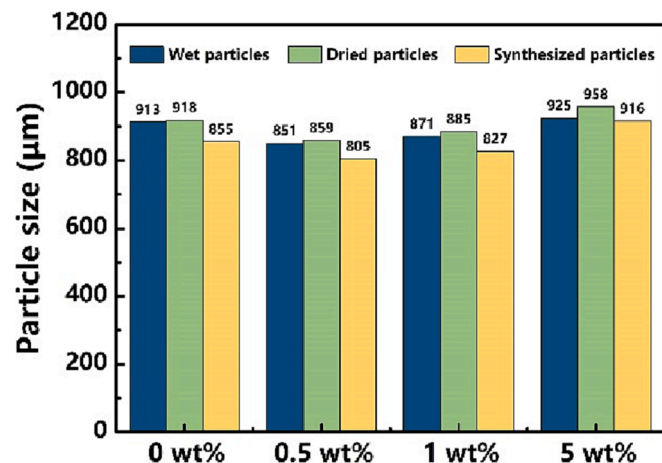


Fig. 5. Particle size of different ratio of SiC-doped materials during particle preparation.

3.2. Analysis of particle size

Particle size test was conducted on wet particles, dried particles, and synthesized particles, as shown in Fig. 5. It can be seen that the particle size changes of the four materials exhibit similar patterns. After drying, the particle size slightly increases due to the evaporation of water. During high-temperature treatment, synthesis of Mn-Fe oxide occurs, and microcrystalline cellulose is carbonized at high temperature, leading to further particle shrinkage and a decrease in particle size after high-temperature treatment. Particle size distribution data are provided in the Supporting Information.

4. Attrition characteristic

To investigate the attrition of Mn-Fe particles in CSP plants, it is necessary to first analyze their dissipated energy and attrition ratio based on attrition characteristic tests. Based on this, a correlation can be established with the attrition process in CSP plants.

4.1. Model of dissipated energy of particles attrition

When particles collide, energy dissipation mainly occurs in the contact area between the particle and the impacted surface. Part of the energy is used to change the kinetic energy of both the particle and the impacted surface. When particles slide, energy dissipation mainly occurs in the frictional contact area between the particle and the sliding surface. The energy is consumed to overcome the resistance caused by friction. These indicate that attrition is essentially an energy dissipation problem [24]. Huq, Celis, Fouvry, Mohrbacher, and others have proposed methods to calculate attrition volume and verified a linear relationship between attrition volume V and dissipated energy E expressed as Eq. (1) [17,25–26,33].

$$V = K_c E \quad (1)$$

Here, K_c is the factor which describes the volume of attrition per unit of energy consumed. The exact value depends on factors such as the physical properties, the attrition conditions and the test method. In subsequent calculations, the K_c value is assumed to be equal.

Archard considers the plasticized contact between materials where the contact area is the ratio of the normal force to the material hardness, and defined the frictional attrition volume loss V_{fric} as Eq. (2) [5].

$$V_{fric} = \frac{k_f NL}{3 H_f} = K_{fric} \hat{A} \cdot L \cos \theta_N \quad (2)$$

Here, k_f is the coefficient showing the probability that the micro protrusions on the surface will be sheared off, N is the normal force, L is the relative sliding distance, H_f is the hardness of the particles and θ_N is the angle between force and normal direction. K_{fric} is coefficient of the frictional attrition volume loss. In subsequent calculations, the K_{fric} value is assumed to be equal.

In impact attrition analysis, the volume loss can be defined by sub-surface transverse cracks, and free surfaces can easily be separated from the impact site to form particle fines. [29]. Based on indentation fracture mechanics, the volume of particle fines can be estimated from the depth and length of transverse cracks. Accordingly, they propose the Eq. (3) to estimate the impacted attrition volume loss V_{imp} [18].

$$V_{imp} = k_{imp} \frac{\rho v_{imp}^2 l^4 H_f}{K_{ft}^2} = K_{imp} \hat{A} \cdot v_{imp}^2 \quad (3)$$

Here, k_{imp} is the proportionality factor, the properties of the particle including density ρ , linear particle size l , hardness H_f , fracture toughness K_{ft} , and the normal velocity v_{imp} . K_{imp} is coefficient of the impacted attrition volume loss. In subsequent calculations, the K_{imp} value is assumed to be equal.

The cumulative dissipated energy of a single particle circulating in

the cylindrical drum is as Eq. (4).

$$E_{sum} = E_{imp} + E_{fric} \quad (4)$$

The cumulative energy E of Mn-Fe particles in the cylindrical drum was simulated using EDEM software based on particles movement analysis. The simulation parameters, such as the device size, particle sphericity, particle size, and particle friction coefficient, were set to be consistent with those of the experimental apparatus and actual particles characteristics. The contact model between the particles and the wall was based on the Hertz-Mindlin model, with standard rolling friction and relative attrition models employed as additional models [38]. The cumulative energy E due to particle impact and friction acting on the inner wall and baffle wall of the cylinder was estimated, and the degree of attrition was quantified accordingly.

4.2. Analysis of particle attrition in the cylindrical drum

The process and simulation results of one rotation cycle (1 s) of the particles in the cylindrical drum are shown in Fig. 6. During each rotation cycle, most particles undergo two collisions with the cylinder, as indicated in Fig. 6a–d for the first collision, and Fig. 6e–h for the second collision. As shown in Fig. 6a–d, the particles fall from the top surface under gravity, collide with the bottom surface and experienced their first collision with the inner wall. The height of the particle's initial position affects its landing point, with a wide range of possible landing points. As shown in Fig. 6e–f, after falling to the bottom, the particles move towards the middle of the cylinder due to static friction, maintaining a relatively thin layer without significant accumulation. As shown in Fig. 6g, when the frictional force is insufficient to support further upward movement, the particle begins to fall again, colliding with the baffle, resulting in the second collision. As shown in Fig. 6h, the particle forms an accumulation pile under the push of the baffle and continues to move upward. This is reflected in the layer of particles, which becomes thicker from the middle position, eventually stabilizing in thickness, completing one cycle. The observed patterns of two collisions match well with the simulation results. To facilitate calculation, the movement of the particles in the cylindrical drum was simplified as follows: the particles fall to the bottom under gravity, experience the first attrition (impact attrition), then move towards the middle of the cylindrical drum, where the frictional force is insufficient to support them, causing relative displacement (friction attrition), before colliding with the baffle for the second time (impact attrition). Finally, pushed by the baffle, they move towards the top, completing a cycle.

As shown in Fig. 7a, the average velocity of particles in the

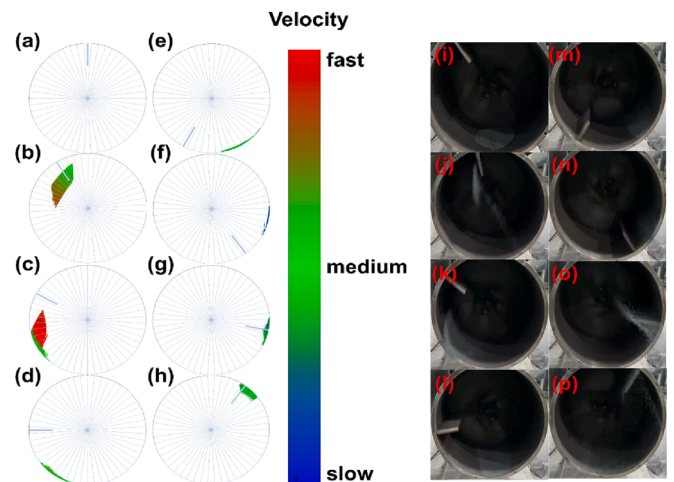


Fig. 6. One rotation cycle of the particles in the cylindrical drum: (a)–(h) simulation results of attrition test and (i)–(p) rotation process.

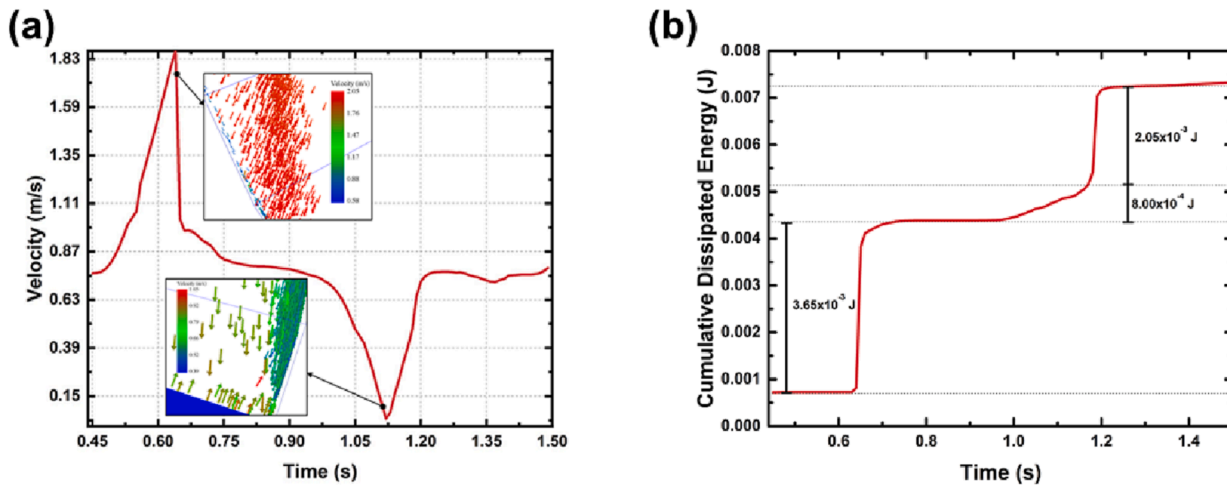


Fig. 7. (a) Average velocity of particles in the cylindrical drum. (b) The cumulative dissipated energy.

cylindrical drum was obtained through simulation. The first collision of two collisions can be regarded as the particle falling from a height D (the inner diameter of the cylindrical drum) and colliding with the cylindrical wall, with the velocity increasing from 0.76 m/s to 1.87 m/s and then the velocity falling back after the collision. The second collision occurs when the particle collides with the baffle. When the particle reaches the middle of the cylinder, it no longer continues to move upward with the cylinder, and its velocity gradually decreases from 0.76 m/s to 0. Subsequently, under the influence of gravity, the particle slides downward and its velocity gradually increases. The velocity before colliding with the baffle is 0.32 m/s.

As shown by two particle flow field in Fig. 7a, the angle between the particle and the wall of the cylindrical drum at the first collision is about 55°, and the particle is nearly perpendicular to the baffle at the second collision, and the particle is hedged against the baffle, and the sum of the rates of the particle and the baffle is considered to be the normal velocity. The velocities of the two collisions are 1.53 and 1.18 m/s, respectively. As shown in the Fig. 7b, the collisions of the particle were simulated and the cumulative dissipated energy was calculated. Analysis of particle motion reveals that average impacted attrition dissipated energy of the two collisions are 3.65×10^{-3} J and 2.05×10^{-3} J per rotation, while average frictional attrition dissipated energy is 8.00×10^{-4} J per rotation. The cumulative attrition energy E_{sum} for one hour is 23.4 J. The impacted volume loss per rotation V_{imp} is $3.74 K_{imp}$, whereas the volume loss attributed to frictional attrition V_{wear} is $4.30 \times 10^{-2} K_{fric}$.

4.3. Results of long-term attrition characteristic test

Long-term attrition characteristics were characterized via a com-

parison of attrition rates (AR) and remaining mass ratios (MR). Explanations and calculation methods for AR and MR are provided in the Supporting Information. Undoped Mn-Fe particles prepared in this study exhibited a high attrition rate, with a mass loss of approximately 55.4% after 120 h of attrition test in cylindrical drum apparatus. To enhance the attrition resistance, three types of SiC-doped Mn-Fe particles were prepared and subjected to a total of 120 h of attrition test, equivalent to 4.32×10^5 rotations. As shown in Fig. 8, the with 5% SiC doped particle had an attrition rate of 0.0417%/h and mass loss of 3.26% after 120 h. Although 0.5% SiC doped exhibited a higher attrition rate during the initial 8 h, the attrition rate decreased significantly after 20 h test, with a final attrition rate of 0.0281%/h and mass loss of 5.00% after 120 h test. The attrition characteristics of 1% SiC doped particles was further improved, with an attrition rate of 0.0156%/h and mass loss of 1.87% at 120 h. SiC-doped Mn-Fe particles showed a significant improvement in attrition resistance compared to the original Mn-Fe particles.

4.4. Analysis of the reinforcement mechanism for SiC-doped particles

During attrition test, particles are susceptible to fracture due to the impact of attrition mechanisms, resulting in the formation of several sub-particles of similar size to the parent particle, or delamination wear, in which surface edges, protrusions, depressions, and other features are gradually worn down or chipped away, forming small particles and particle fines [50]. The attrition process is the gradual breaking of particles or detachment of surface layers, and their attrition resistance is not related to their hardness, but rather depends on their material toughness [37]. When the SiC doping ratio was increased from 0.5 wt% to 1 wt%, its attrition resistance was enhanced. Based on Fig. 9(a)-(b),

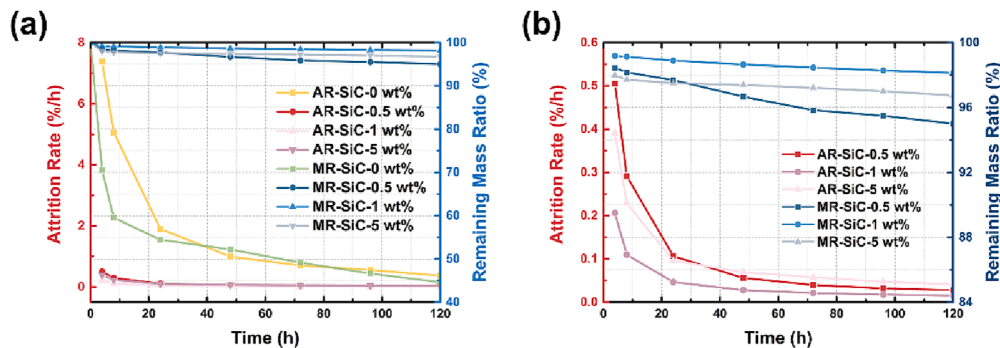


Fig. 8. Attrition rate and remaining mass ratio of (a) all Mn-Fe particles and (b) SiC-doped Mn-Fe particles.

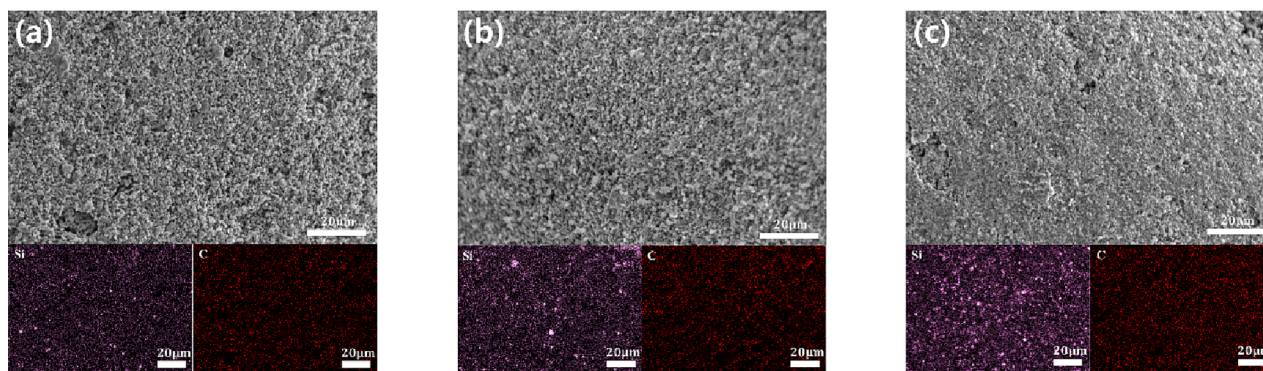


Fig. 9. SEM images and corresponding EDS elemental mappings of (a) 0.5 wt%, (b) 1 wt%, (c) 5 wt%.

the reason for this can be analyzed: the distribution density of SiC in Mn-Fe particles gradually increases, and since SiC has a high Peierls stress, it can resist lattice distortion, while SiC crystal grains can offset cracks during the fracture process, impeding crack development and improving the attrition resistance of Mn-Fe particles. However, when the SiC ratio was increased from 1 wt% to 5 wt%, based on Fig. 9(b)-(c), the reason for the decrease in attrition resistance can be analyzed. Due to the higher activity of SiC, excessive doping may cause aggregation during powder preparation, resulting in flocculation in particles, leading to the formation of defects such as pores, dislocations, and stress concentration, providing a path for crack propagation and reducing particle attrition resistance [37]. This is also consistent with the results of attrition tests, as the initial attrition rate for 5 wt% particles was slower than for 0.5 wt% particles. As attrition proceeded and cracks developed, the attrition rate for 5 wt% particles became faster than for 0.5 wt% particles.

4.5. Results of particle size distribution of long-term attrition characteristic test

During attrition characteristic tests, the average size of particles gradually decreases due to attrition. Some particles become too small to flow when their size decreases below the mesh size, rendering them unsuitable for use. Therefore, the attrition characteristic test is based on changes in particle size distribution. There exists a close relationship between changes in particle size distribution and attrition characteristics, highlighting the need for further research on particle size distribution.

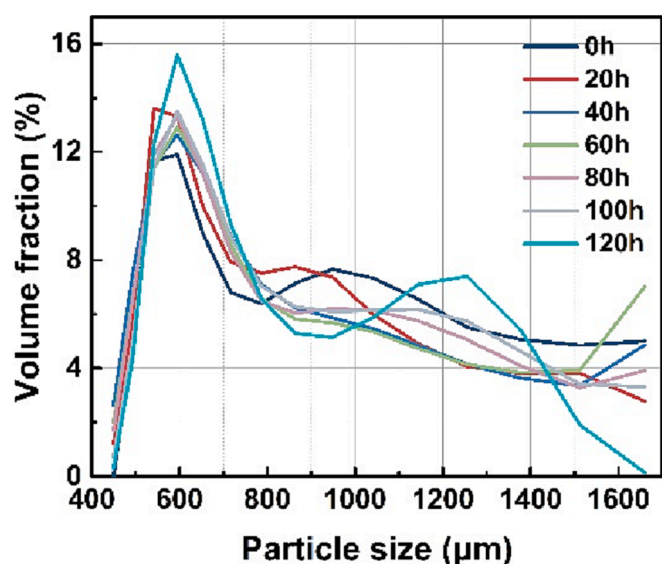


Fig. 10. 0.5 wt% SiC-doped particle size distribution of different attrition test.

As shown in Fig. 10, this study examined the particle size distribution of 0.5 wt% SiC-doped Mn-Fe particles after attrition tests. The particles had a wide particle size distribution with a median particle size of 805 μm and were divided into 16 particle size intervals, each characterized by its midpoint. After 120 h of attrition testing, the median particle size was 748 μm . The smallest size interval is composed of particles sieved. At the beginning of attrition, the transition from large particle size intervals (1199–1741 μm) to intermediate (623–1198 μm) and small particle size intervals (<622 μm) was dominant, resulting in an increase in the proportion of particles in the intermediate and small particle size intervals. As attrition continued, the transition from intermediate particle size intervals to small particle size intervals and even the sieving interval became dominant, resulting in a gradual decrease in the proportion of particles in the intermediate particle size interval. The particle size intervals that dominated the transition in the particle size distribution were different, resulting in the change in the distribution pattern not remaining constant over time.

The results of particle size distribution indicate that the highest proportion of 0.5 wt% SiC-doped Mn-Fe particles' transformation occurs in the size range of 568–750 μm . This suggests that the attrition mechanism of the particles during the long-term attrition test is mainly dominated by fragmentation.

5. Reaction performance

5.1. Reaction characterization of different SiC-doped ratio

The XRD patterns of different SiC-doped Mn-Fe particles are shown in Fig. 11(a). All synthesized samples exhibit distinct reflections of (Mn, Fe)₂O₃ (bixbyite, ICDD 00-041-1442), indicating a uniform formation of the continuous solid solution. The XRD patterns of SiC-doped samples show peak of SiC (Synthetic, ICDD 97-002-4217). Due to the low content of SiC, its peak is not very significant, as further demonstrated in Fig. 11 (b)-(c).

To investigate the effect of SiC doping on the reaction performance of Mn-Fe particles, the reduction and oxidation reaction performance of Mn-Fe particles doped with different ratio of SiC were compared in the first cycle, as shown in Fig. 12. As the SiC doping proportion increased, the particles maintained a relatively fast reaction rate, achieving rapid oxidation and reduction. However, the conversion of the strength particles gradually decreased, with maximum conversion of 95.7%, 90.4%, and 33.7% for 0.5%, 1%, and 5% SiC doping, respectively. The particles doped with 0.5% and 1% SiC showed better reaction performance than those doped with 5% SiC. All strength particles exhibited good re-oxidation ability, with almost complete re-oxidation of the reduced portion.

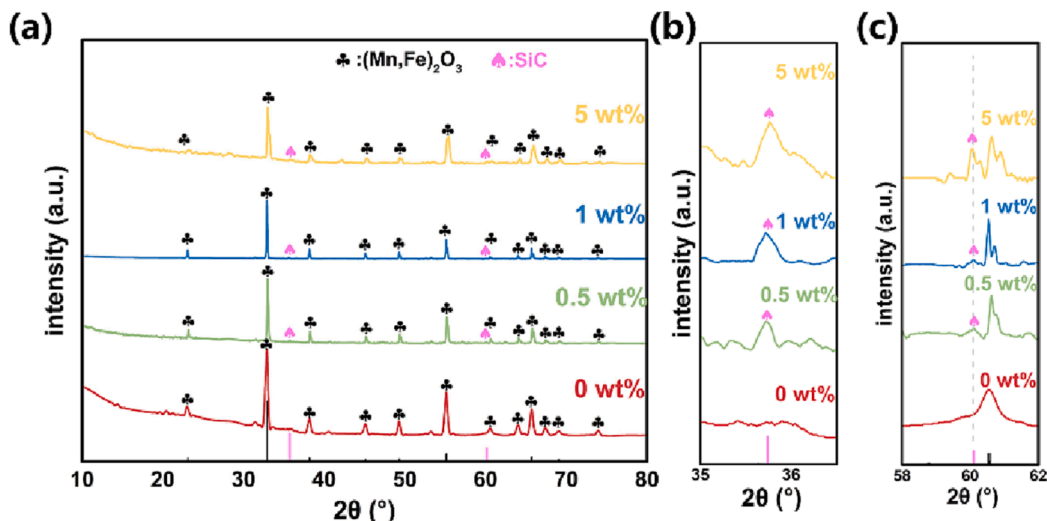


Fig. 11. XRD patterns of Mn-Fe particles doped with different ratios of SiC. (a) 10° – 80° , (b) 35° – 36.5° , (c) 58° – 62° .

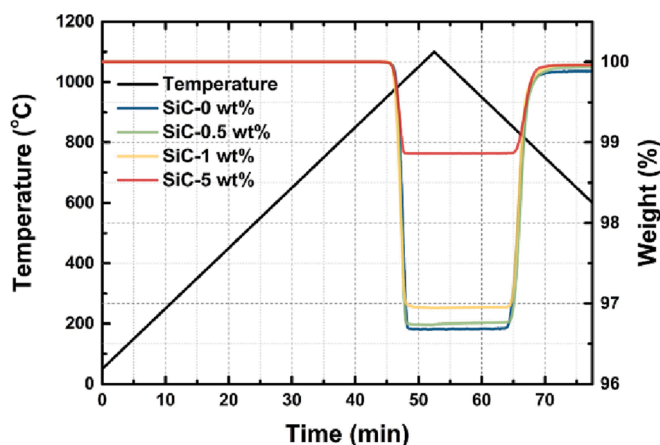


Fig. 12. Reaction performance comparison of different SiC-doped Mn-Fe particles.

5.2. Results of cycling performance

To investigate the evolution in reaction cycling performance of Mn-Fe particles doped with 0%, 0.5%, and 1% SiC after long-term cycling, 800 cycles were performed. The XRD patterns of different SiC-doped Mn-Fe particles after cycling test are presented in Figs. S1–S3 of the Supporting Information. The results demonstrate that SiC can exist stably in Mn-Fe particles during long-term cycling processes. The undoped Mn-Fe particles and those doped with 0.5% and 1% SiC showed a decrease of the oxidation conversion after the 800th cycle, to 87.4%, 91.7%, and 82.3%, respectively. As power generation and heat release are directly related, the evolution of the oxidation performance during the cycles was further fitted, as shown in Fig. 13(d). The long-term cycling of all three types of particles exhibited a trend of initially fast and then slow deterioration in oxidative reactivity.

6. Replenishment model for CSP plants

6.1. Models of replenishment strategy for CSP plants

In CSP plants, the gradual decrease in mass of Mn-Fe particles due to fine particle sieving, coupled with their deteriorating redox reaction performance over time, results in a decline in heat storage capacity. Thus, the particle replenishing is necessary. Furthermore, for particles

strengthen through doping, although their attrition resistance performance improves, their reaction performance gradually decreases. Selecting the appropriate particle type presents a challenge, necessitating the introduction of a new indicator for comprehensive evaluation. The total replenishment mass over long-term operation can provide an intuitive reference for particle type selection. Moreover, due to non-uniform deterioration rates of mass loss and reaction performance, replenished particles will be at different stages of evolution, resulting in varying loss rates. This further complicates the periodic replenishment process, underscoring the need to develop effective replenishment strategies.

The remaining heat storage capacity of particles before the n_t replenishment can be calculated using Eq. (5) as follows:

$$H_{remain,t} = H_0 \hat{\Delta} \sum_{i=0}^{n_t-1} \alpha_{m,i,t} \hat{\Delta} \alpha_{h,i,t} \quad (5)$$

Here, H_0 is the initial heat storage capacity of particles, n_t represents the i_{th} replenishments, $\alpha_{m,i,t}$ and $\alpha_{h,i,t}$ represents the remaining mass ratio and the remaining heat storage capacity ratio of the i_{th} replenishment particles before the n_t replenishment. When $i = 0$, it corresponds to the addition of original particles into the system.

The calculation of α_h is as follows:

$$\alpha_h = \frac{H_{TCE} + H_{SH,0}}{H_{TCE,0} + H_{SH,0}} \quad (6)$$

Here, H_{TCE} is the current heat storage capacity of the thermochemical reaction, which is proportional to the conversion of the oxidation. $H_{TCE,0}$ is the original thermochemical heat storage density (oxidation reaction enthalpy), set as 202 kJ/kg. And $H_{SH,0}$ is the original sensible heat storage density, set as 525 kJ/kg (400–1000 °C).

To maintain the system's heat storage capacity at the design value by replenishing particles, the required replenishment mass corresponds to the heat storage capacity ΔH_{n_t} as shown in Eq. (7).

$$\Delta H_{n_t} = H_0 - H_{remain,n_t} \quad (7)$$

The heat storage replenishment ratio compared to the original heat storage capacity k_{H,n_t} is calculated as Eq. (8).

$$k_{H,n_t} = \frac{\Delta H_{n_t}}{H_0} \quad (8)$$

The calculation of the replenishment mass of particles Δm_{n_t} is as Eq. (9).

$$\Delta m_{n_t} = \frac{\Delta H_{n_t}}{H_{TCE,0} + H_{SH,0}} \quad (9)$$

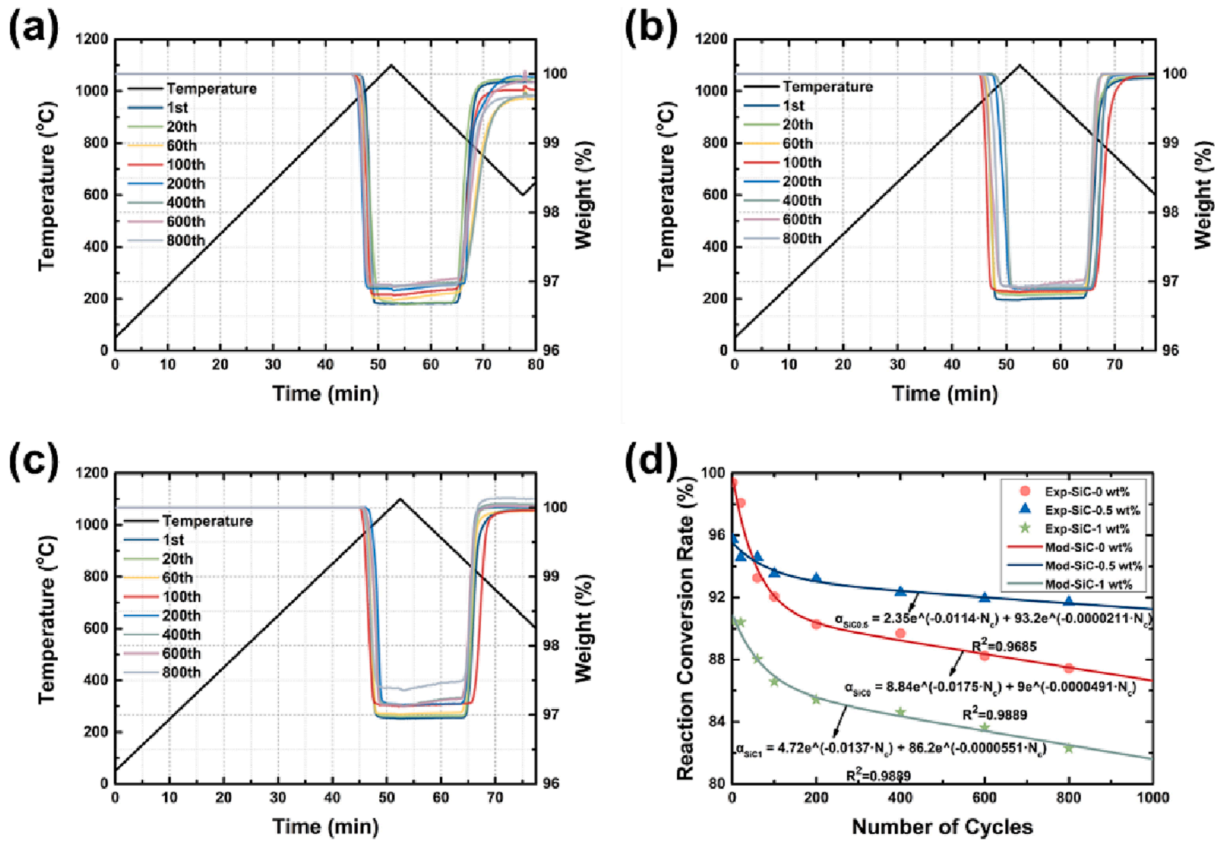


Fig. 13. Long-term reaction performance test of SiC-doped Mn-Fe particles. (a) 0 wt% (b) 0.5% wt.% (c) 1%, (d) fitting curve.

The total mass of particles in the system after replenishment m_{n_t} is as follows,

$$m_{n_t} = m_{remain,n_t} + \Delta m_{n_t} \quad (10)$$

Here, m_{remain,n_t} is the remaining particle mass before the n_t th replenishment.

The replenishment mass ratio k_{m,n_t} compared to the original mass is calculated as Eq. (11).

$$k_{m,n_t} = \frac{\Delta m_{n_t}}{m_0} \quad (11)$$

Here, m_0 is the original total mass.

The total replenishment mass ratio in the system k_{sum_m,n_t} is expressed as Eq. (12).

$$k_{sum_m,n_t} = \sum_{i=1}^{n_t} k_{m,n_t} \quad (12)$$

The average annual replenishment rates $k_{rep,annu}$ is calculated as follow,

$$k_{rep,annu} = \frac{k_{sum_m,n_t}}{n_{year}} \quad (13)$$

Here, n_{year} is operation year.

6.2. Models of attrition conversion factor of CSP plants

To further analyze particle attrition in CSP plants and obtain dissipated energy of attrition, it is necessary to calculate the energy dissipation processes of particles in each device [4,12,19]. Circulating particles flow through the particle receiver, hot particle storage, heat exchanger, cold particle storage, particle elevator, and interconnecting pipelines. As particle attrition differs among devices, their attrition processes must be analyzed separately. The analysis of particle flow and

reaction processes, as well as the calculation of dissipated energy in CSP plants, are presented in the Supporting Information. The sum of attrition for all devices represents the accumulated attrition.

To establish a correlation between attrition characteristics obtained from the cylindrical drum attrition characteristic test apparatus and attrition processes in CSP plants, this study proposes an attrition conversion factor R by analyzing the energy dissipation of both attrition processes. With coefficient R, attrition process of particles in CSP plants can be predict based on long-term attrition test from cylindrical drum attrition characteristic test apparatus. R is defined as the ratio of attrition time of particles between the CSP plant and the cylindrical drum attrition characteristic test apparatus, which can also be defined as the ratio of dissipated energy of attrition, as shown in Eq. (14).

$$R = \frac{\dot{E}_{CSP}}{\dot{E}_{cyl}} = \frac{\dot{V}_{CSP}}{\dot{V}_{cyl}} \quad (14)$$

Here, \dot{E}_{CSP} is the total dissipated energy of particle attrition of CSP plant, and \dot{E}_{cyl} is of cylindrical drum, \dot{V}_{CSP} is the total volume loss of particle attrition of CSP plant, and \dot{V}_{cyl} is of cylindrical drum.

To analyze the attrition of Mn-Fe particles in CSP plants, this study focused on the 125 MWe CSP plant designed by Buck et al. [12]. The dissipated energy and volume loss of each equipment were calculated based on the its geometric parameters of and the flow process of particles. The total dissipated energy of attrition of the CSP plant and the conversion factor R were obtained.

For the 125 MWe CSP system, a multi-tower configuration consisting of 14 solar tower modules is used. The storage capacity of a single module is 249 MWh, and the designed power of the absorber is 50 MW_{th} [12]. The system also includes a heliostat field (869 heliostats), heat exchanger, and storage and transport system. The geometric parameters, attrition volume loss, and attrition dissipated energy are listed in Table S1, Supporting Information. The attrition conversion factor of 125

MWe system $R_{125\text{MWe}}$ is 0.0780.

6.3. Replenishment strategy for 125 MW CSP plants

To ensure that the heat storage capacity of particles in the system meets operational requirements, this study analyzed particle replenishment strategies, including particle replenishment rates and total replenishment mass ratio, for undoped, 0.5% SiC-doped, and 1% SiC-doped Mn-Fe particles in 125 MWe CSP systems. The analysis relied on an attrition conversion factor R , particle reaction performance evolution, and attrition characteristic evolution, all integrated into a particle replenishment model. The original particle storage corresponds to a 12-hour storage capacity [12], and the particles undergo one flow cycle and one reaction cycle per day in the system, with daily replenishment. The total operating time is 25 years [12]. The calculation results are presented in Fig. 14.

As shown in Fig. 14(a) and (b), for the 125 MWe CSP system, the particle replenishment rates of particles gradually decrease and eventually stabilize, while the total replenishment mass ratio initially increases rapidly and gradually tends to linear growth. The particle replenishment rates for undoped, 0.5% SiC-doped, and 1% SiC-doped Mn-Fe particles stabilize at 3.04×10^{-4} , 2.87×10^{-5} , and 1.69×10^{-5} per day, respectively. And the total replenishment mass ratio over the 25-year are 3.56 times, 0.316 times, and 0.248 times the original total particle mass (excluding the original total particle mass), with average annual replenishment rates $k_{\text{rep,annu}}$ [19] of 1.43×10^{-1} , 1.26×10^{-2} , and 9.94×10^{-3} , respectively.

It can be observed that the SiC-doped Mn-Fe particles show a significant decrease in particle replenishment rates and total replenishment mass ratio, both of which decrease by approximately one order of magnitude after SiC doping reinforcement. This is beneficial for reducing the cost of particle inventory and improving the LCOE of the system [9,12,23]. Since this study focuses on the replenishment strategy, and the influence of SiC doping on storage capacity is relatively small, the analysis mainly revolves around the amount of replenishment. If the worn particles are sieved and recycled to regenerate new particles, the cost of replenishment can be further reduced. Assuming that the cost of Mn-Fe particle fabrication is 10% of the material cost, and based on the research of Buck et al. [12], the break-even prices were further corrected to 1.606, 1.221 and 1.213 €/kg for undoped, 0.5% SiC-doped, and 1% SiC-doped Mn-Fe particles of 125 MWe CSP system. It can be seen that compared with undoped particles, adopting strengthen particle can significantly reduce the cost of particle inventory.

6.4. Further research based on replenishment model

To further analyzing the influence of different factors on particle

replenishment of CSP plants, this study focuses on three key parameters: reaction cycling performance, attrition characteristic, and reaction enthalpy. With the superior properties of 0.5 wt% and 1 wt% SiC-doped Mn-Fe particles as shown above, the replenishment process of both particles under different parameters was analyzed and compared based on 125 MW CSP plant.

6.4.1. Reaction cycling performance deterioration rate

Based on the reaction cycling performance of SiC-doped particles, eight groups of deterioration rates ranging from $0.1 \times$ to $10 \times$ were set up for comparison. Here, $10 \times$ represents a deterioration rate where the deterioration ratio of reaction cycling performance after one redox reaction is equivalent to that of ten times the original reaction (Mn-Fe particles), indicating an accelerated deterioration based on time, rather than a simple ten times loss ratio. Similarly, $0.1 \times$ represents a deterioration ratio where the deterioration ratio of ten reactions is equivalent to that of one single original reaction (Mn-Fe particles).

As shown in Fig. 15, the total replenishment mass ratio of both particles will gradually increase as the deterioration rate of reaction cycling performance increases from $0.1 \times$ to $10 \times$. This is easily understandable since, as the deterioration rate of reaction cycling performance accelerates, the system's heat storage capacity also decreases faster, resulting in an increasing need for replenishment. Furthermore, at different deterioration rates, the total replenishment mass ratio of 1 wt% SiC-doped particle is always lower than that of 0.5 wt%.

6.4.2. Attrition characteristic

Based on the attrition characteristic of SiC-doped particles, eight groups of attrition rates ranging from $0.1 \times$ to $10 \times$ were compared. The meaning of attrition rate is similar to deteriorate rate mentioned above. As shown in Fig. 16, as the attrition rate increases from $0.1 \times$ to $10 \times$, the total replenishment mass ratio of both particles gradually increases similarly to the previous section. However, when the deteriorate rate is relatively small, the total replenishment mass ratio of 0.5 wt% SiC-doped particles is lower than that of 1 wt%, as the reaction performance deterioration plays the dominant impact when the attrition rate slows down. In this case, the reaction cycling performance of 0.5 wt% particles were superior to that of the 1 wt%, leading to less particle replenishment. As the attrition rate accelerates, attrition characteristic predominates, and thus the total replenishment mass ratio of 1 wt% particles become relatively less.

6.4.3. Reaction enthalpy

As a key parameter of TCES materials, it is necessary to analyze the impact of reaction enthalpy on the replenishment process. As shown in Fig. 17(a)–(c), the total replenishment mass ratio is calculated based on the initial particles adding into the system. It can be seen that as the

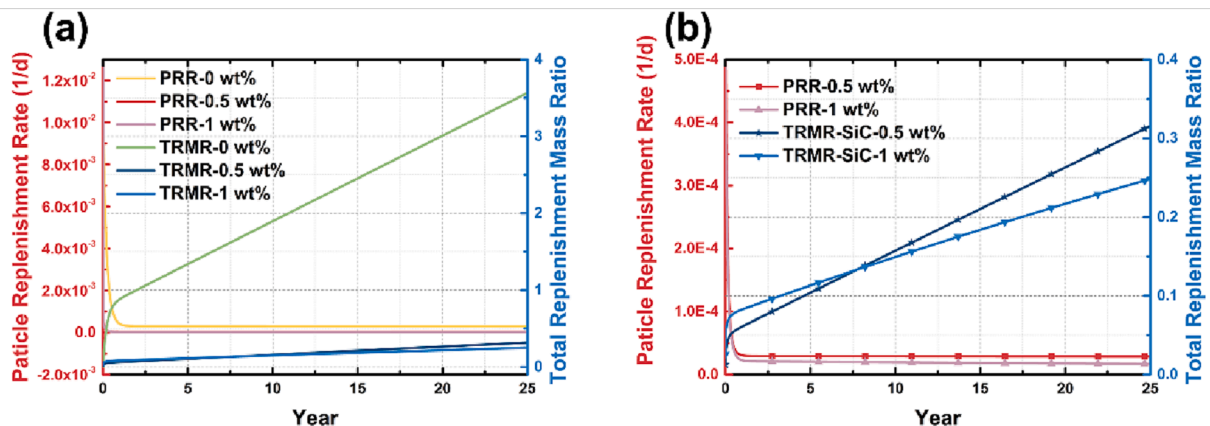


Fig. 14. Particle replenishment of (a) all Mn-Fe particles of 125 MW CSP system, (b) SiC-doped Mn-Fe particles of 125 MW CSP system.

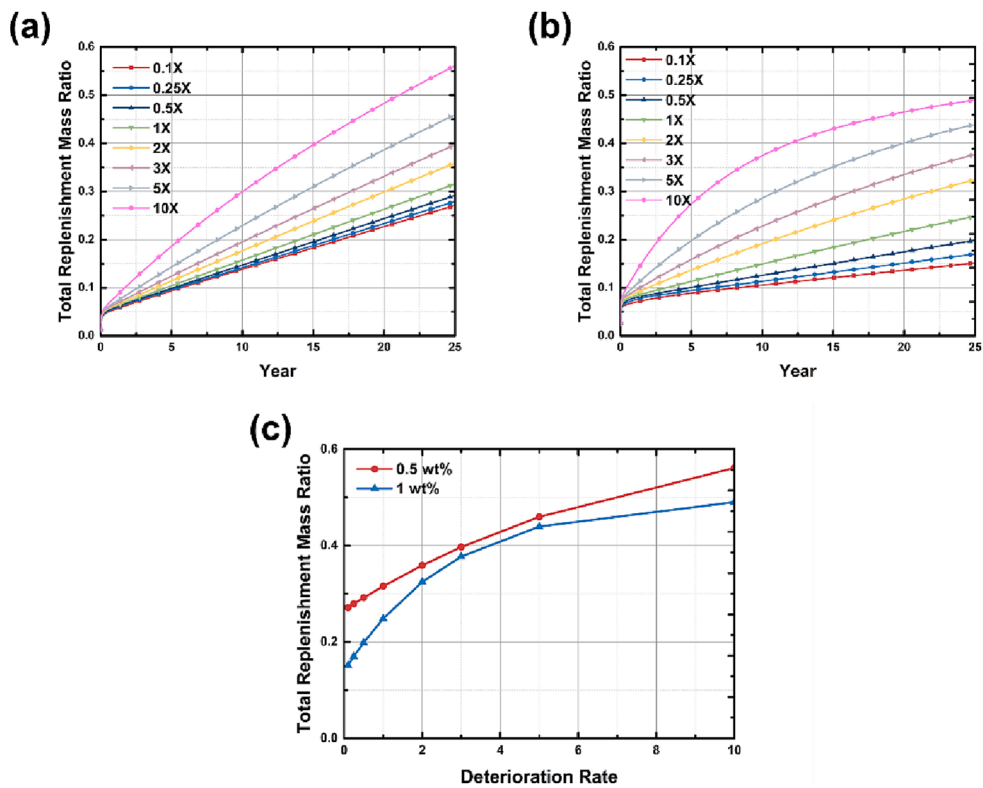


Fig. 15. Total replenishment mass ratio under different reaction cycling performance deteriorate rates. (a) 0.5 wt%, (b) 1 wt%, (c) Comparison.

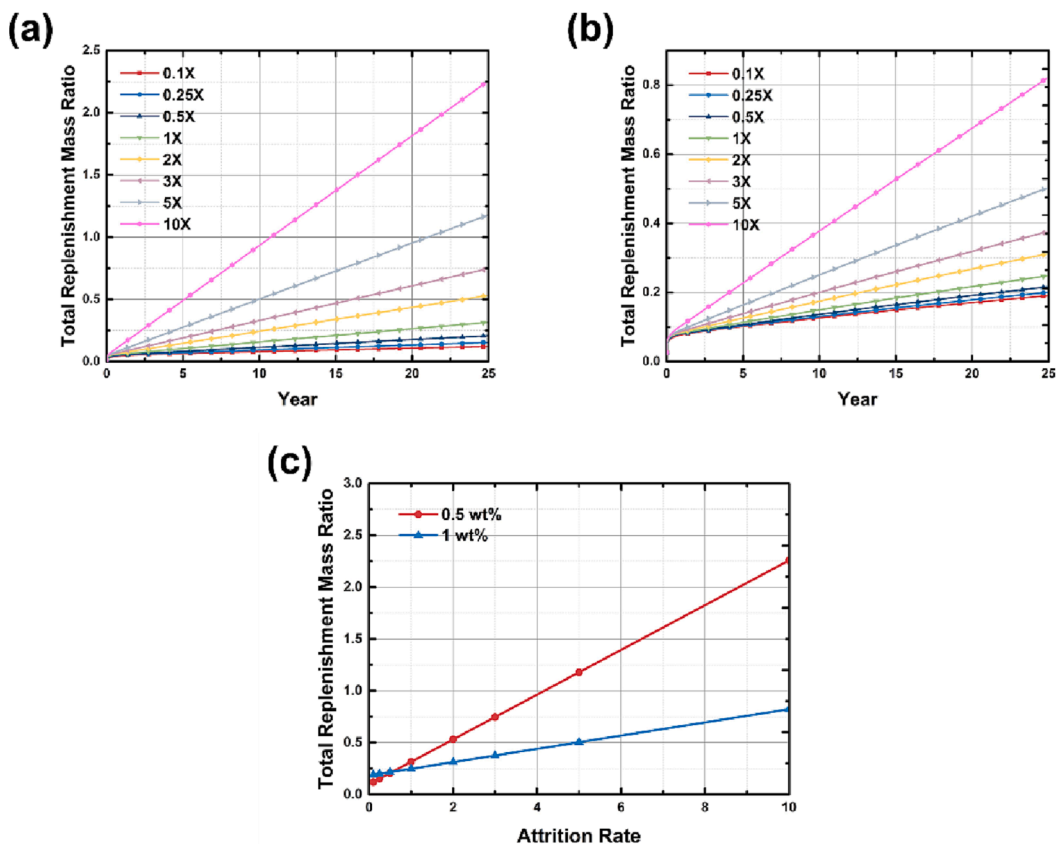


Fig. 16. Total replenishment mass ratio under different attrition characteristic. (a) 0.5 wt%, (b) 1 wt%, (c) Comparison.

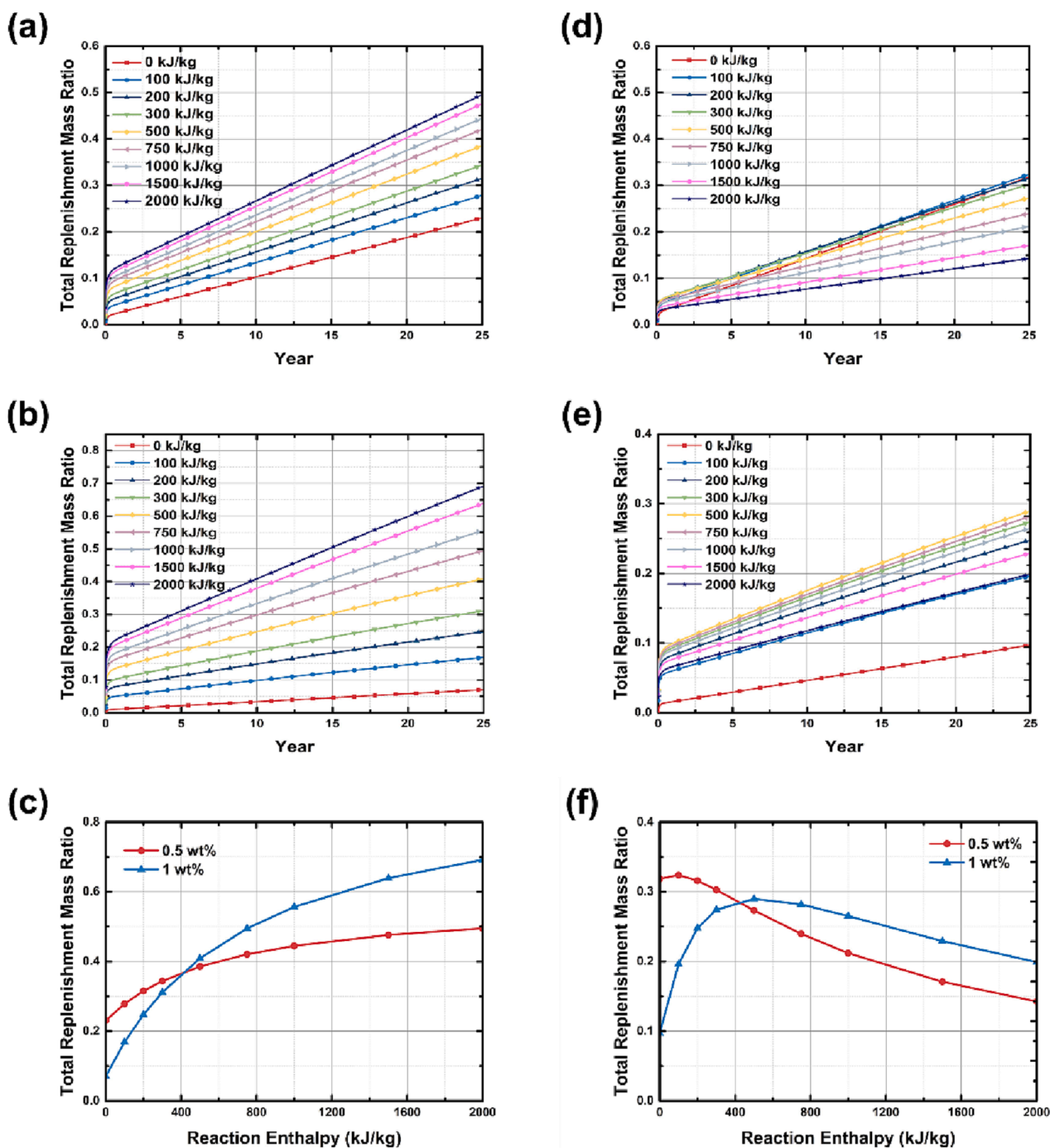


Fig. 17. Total replenishment mass ratio under different reaction enthalpy. Based on the initial particles, (a) 0.5 wt%, (b) 1 wt%, (c) Comparison. Based on the initial mass of Mn-Fe particles, (d) 0.5 wt%, (e) 1 wt%, (f) Comparison.

reaction enthalpy increases, the proportion of replenishment relative to the initial particle mass gradually increases. This is because the higher the reaction enthalpy, the higher its proportion in thermal energy storage density. Under the same reaction cycling performance deterioration rate, the loss of system's heat storage capacity is also greater, and the required particle supplementation is also correspondingly higher. Based on Fig. 17(c), it can be seen that when the reaction enthalpy is relatively low (<420 kJ/kg), 1 wt% SiC-doped particles have an advantage. As the reaction enthalpy further increases, 0.5 wt% SiC-doped particles are more advantageous. The total replenishment mass ratio in Fig. 17(d)–(e) is calculated based on the initial mass of Mn-Fe particles in the system. Referring to Fig. 17(e), similarly, when the

reaction enthalpy is relatively low, 1 wt% SiC-doped particles have an advantage. After further increasing the reaction enthalpy, 0.5 wt% SiC-doped particles are more advantageous. However, the total replenishment curve is not monotonically increasing, showing a trend of first increasing and then decreasing. This is because when the reaction enthalpy is relatively low, the increase in energy density results in a smaller proportion of decrease in the total particle mass, while the growth rate of particle replenishment due to the loss of reaction performance is faster. As the reaction enthalpy keeps increasing and reaches the peak of total replenishment mass ratio, the increase in energy density results in a higher proportion of decrease in the total replenishment mass, while the corresponding proportion of particle replenishment due

to the loss of reaction performance decreases, resulting in a changing trend as shown in Fig. 17(e).

7. Conclusion

SiC-doped Mn-Fe particles with varying doping ratios demonstrated improved attrition resistance and long-term reaction cycle characteristics, which are advantageous for the long-term stable operation and economic improvement of CSP systems. Doping at 0.5 wt%, 1 wt%, and 5 wt% resulted in mass loss ratios of 5.00%, 1.87%, and 3.26% (120 h test), respectively, compared to the undoped Mn-Fe particle's mass loss of 53.5% (96 h test). Additionally, undoped and 0.5% and 1% SiC-doped particles exhibited good cycle performance, with oxidation conversion of 87.4%, 91.7%, and 82.3%, respectively, after 800 cycles. However, increased strength through doping led to decreased reaction performance, posing a challenge for selecting particles in CSP systems. To address this issue, a new indicator was proposed: the total replenishment mass ratio. Correlation analysis between attrition testing and CSP system flow process underpins the replenishment strategies required to maintain heat storage capacity. Simulation-based studies on attrition volume loss and energy dissipation provided insights into the relationship between attrition characteristics and the CSP system operation. Based on replenishment strategy, strengthened Mn-Fe particles showed reduced replenishment rates by one order of magnitude relative to undoped particles. Specifically, the average annual replenishment rates were 14.3%, 1.26%, and 0.994% for undoped and 0.5 wt% and 1 wt% SiC-doped Mn-Fe particles, respectively, in a 125 MWe CSP system over a 25-year operation period. This reduction in particle replenishment rates can significantly reduce particle inventory and break-even prices, contributing to a lowered CSP system LCOE and promoting wider use of renewable energy sources.

This study provides crucial insights into the development of thermochemical energy storage, facilitating more extensive utilization of solar energy to meet future energy needs. Improved attrition resistance achieved by SiC-doped Mn-Fe particles can reduce particle fines, ensure continuous particle flow, and lower system replenishment rates, thereby contributing to the wider adoption of renewable energy sources.

Declaration of Competing Interest

The authors declare that they have no known competing financial interests or personal relationships that could have appeared to influence the work reported in this paper.

Acknowledgements

The authors gratefully acknowledge the support from the National Natural Science Foundation of China (No. 52176207), Key R&D Program of Zhejiang (NO. 2022C01043) and the Fundamental Research Funds for the Central Universities (2022ZFJH004).

References

- Abad, A., Mendiara, T., Izquierdo, M.T., de Diego, L.F., García-Labiano, F., Gayán, P., Adánez, J., 2021. Evaluation of the redox capability of manganese-titanium mixed oxides for thermochemical energy storage and chemical looping processes. *Fuel Process. Technol.* 211, 106579 <https://doi.org/10.1016/j.fuproc.2020.106579>.
- Agrafiotis, C., Block, T., Senholdt, M., Tescari, S., Roeb, M., Sattler, C., 2017. Exploitation of thermochemical cycles based on solid oxide redox systems for thermochemical storage of solar heat. Part 6: Testing of Mn-based combined oxides and porous structures. *Sol. Energy* 149, 227–244. <https://doi.org/10.1016/j.solener.2017.03.083>.
- Al-Shankiti, I.A., Ehrhart, B.D., Ward, B.J., Bayon, A., Wallace, M.A., Bader, R., Kreider, P., Weimer, A.W., 2019. Particle design and oxidation kinetics of iron-manganese oxide redox materials for thermochemical energy storage. *Sol. Energy* 183, 17–29. <https://doi.org/10.1016/j.solener.2019.02.071>.
- Almendros-Ibáñez, J.A., Fernández-Torrijos, M., Díaz-Heras, M., Belmonte, J.F., Sobrino, C., 2019. A review of solar thermal energy storage in beds of particles: Packed and fluidized beds. *Sol. Energy* 192, 193–237. <https://doi.org/10.1016/j.solener.2018.05.047>.
- J.F. Archard Research Laboratory, Associated Electrical Industries Limited, Aldermaston, Berkshire, England Contact and Rubbing of Flat Surfaces *Journal of Applied Physics* 24 8 1953 1953 981 988.
- Azimi, G., Leion, H., Mattisson, T., Rydén, M., Sniijkers, F., Lyngfelt, A., 2014. Mn-Fe oxides with support of MgAl₂O₄, CeO₂, ZrO₂ and Y₂O₃-ZrO₂ for chemical-looping combustion and chemical-looping with oxygen uncoupling. *Ind. Eng. Chem. Res.* 53 (25), 10358–10365.
- Azimi, G., Mattisson, T., Leion, H., Rydén, M., Lyngfelt, A., 2015. Comprehensive study of Mn-Fe-Al oxygen-carriers for chemical-looping with oxygen uncoupling (CLOU). *Int. J. Greenhouse Gas Control* 34, 12–24. <https://doi.org/10.1016/j.ijggc.2014.12.022>.
- Bagepalli, M.V., Jeong, S.Y., Brooks, J.D., Zhang, Z.M., Ranjan, D., Loutzenhiser, P. G., 2022. Experimental characterization of extreme temperature granular flows for solar thermal energy transport and storage. *Sol. Energy Mater. Sol. Cells* 248, 112020. <https://doi.org/10.1016/j.solmat.2022.112020>.
- Bayon, A., Bader, R., Jafarian, M., Fedunik-Hofman, L., Sun, Y., Hinkley, J., Miller, S., Lipiński, W., 2018. Techno-economic assessment of solid-gas thermochemical energy storage systems for solar thermal power applications. *Energy* 149, 473–484. <https://doi.org/10.1016/j.energy.2017.11.084>.
- Bielsa, D., Oregui, M., Arias, P.L., 2022. New insights into Mn₂O₃ based metal oxide granulation technique with enhanced chemical and mechanical stability for thermochemical energy storage in packed bed reactors. *Sol. Energy* 241, 248–261. <https://doi.org/10.1016/j.solener.2022.06.010>.
- Bielsa, D., Zaki, A., Arias, P.L., Faik, A., 2020. Improving the redox performance of Mn₂O₃/Mn₃O₄ pair by Si doping to be used as thermochemical energy storage for concentrated solar power plants. *Sol. Energy* 204, 144–154. <https://doi.org/10.1016/j.solener.2020.04.073>.
- Buck, R., Agrafiotis, C., Tescari, S., Neumann, N., Schmücker, M., 2021. Techno-economic analysis of candidate oxide materials for thermochemical storage in concentrating solar power systems. *Front. Energy Res.* 9 <https://doi.org/10.3389/fenrg.2021.694248>.
- Carrillo, A.J., Chinchilla, L.E., Iglesias-Juez, A., Gutiérrez-Rubio, S., Sastre, D., Pizarro, P., Hungria, A.B., Coronado, J.M., 2021. Determining the role of Fe-doping on promoting the thermochemical energy storage performance of (Mn_{1-x}Fe_x)₃O₄ spinels. *Small Methods* 5 (10), 2100550. <https://doi.org/10.1002/smt.202100550>.
- Carrillo, A.J., González-Aguilar, J., Romero, M., Coronado, J.M., 2019. Solar Energy on demand: a review on high temperature thermochemical heat storage systems and materials. *Chem. Rev.* 119 (7), 4777–4816. <https://doi.org/10.1021/acs.chemrev.8b00315>.
- Carrillo, A.J., Serrano, D.P., Pizarro, P., Coronado, J.M., 2016. Understanding redox kinetics of iron-doped manganese oxides for high temperature thermochemical energy storage. *J. Phys. Chem. C* 120 (49), 27800–27812. <https://doi.org/10.1021/acs.jpcc.6b08708>.
- Dizaji, H.B., Hosseini, H., 2018. A review of material screening in pure and mixed-metal oxide thermochemical energy storage (TCES) systems for concentrated solar power (CSP) applications. *Renew. Sustain. Energy Rev.* 98, 9–26. <https://doi.org/10.1016/j.rser.2018.09.004>.
- Fouvry, S., Kapsa, P., Vincent, L., 1996. Quantification of fretting damage. *Wear* 200 (1), 186–205. [https://doi.org/10.1016/S0043-1648\(96\)07306-1](https://doi.org/10.1016/S0043-1648(96)07306-1).
- Ghadiri, M., Zhang, Z., 2002. Impact attrition of particulate solids. Part I: A theoretical model of chipping. *Chem. Eng. Sci.* 57 (17), 3659–3669. [https://doi.org/10.1016/S0009-2509\(02\)00240-3](https://doi.org/10.1016/S0009-2509(02)00240-3).
- Gorman, B.T., Lanzarini-Lopes, M., Johnson, N.G., Miller, J.E., Stechel, E.B., 2021. Techno-economic analysis of a concentrating solar power plant using redox-active metal oxides as heat transfer fluid and storage media. *Front. Energy Res.* 9.
- Guo, R., Takasu, H., Funayama, S., Shinoda, Y., Tajika, M., Harada, T., Kato, Y., 2022. Mechanical stability and heat transfer improvement of CaO-based composite pellets for thermochemical energy storage. *Chem. Eng. Sci.* 255, 117674 <https://doi.org/10.1016/j.ces.2022.117674>.
- Hamidi, M., Wheeler, V.M., Gao, X., Pye, J., Catchpole, K., Weimer, A.W., 2020. Reduction of iron-manganese oxide particles in a lab-scale packed-bed reactor for thermochemical energy storage. *Chem. Eng. Sci.* 221, 115700 <https://doi.org/10.1016/j.ces.2020.115700>.
- Han, X., Wang, L., Ling, H., Ge, Z., Lin, X., Dai, X., Chen, H., 2022. Critical review of thermochemical energy storage systems based on cobalt, manganese, and copper oxides. *Renew. Sustain. Energy Rev.* 158, 112076 <https://doi.org/10.1016/j.rser.2022.112076>.
- Heller, L., Glos, S., Buck, R., 2022. Techno-economic selection and initial evaluation of supercritical CO₂ cycles for particle technology-based concentrating solar power plants. *Renew. Energy* 181, 833–842. <https://doi.org/10.1016/j.renene.2021.09.007>.
- Hu, Y.-Z., Ma, T.-B., Wang, H., 2013. Energy dissipation in atomic-scale friction. *Friction* 1 (1), 24–40.
- Huq, M.Z., Celis, J.P., 1997. Reproducibility of friction and wear results in ball-on-disc unidirectional sliding tests of TiN-alumina pairings. *Wear* 212 (2), 151–159. [https://doi.org/10.1016/S0043-1648\(97\)00167-1](https://doi.org/10.1016/S0043-1648(97)00167-1).
- Huq, M.Z., Celis, J.P., 2002. Expressing wear rate in sliding contacts based on dissipated energy. *Wear* 252 (5), 375–383. [https://doi.org/10.1016/S0043-1648\(01\)00867-5](https://doi.org/10.1016/S0043-1648(01)00867-5).
- Imran Khan, M., Asfand, F., Al-Ghamdi, S.G., 2023. Progress in research and technological advancements of commercial concentrated solar thermal power plants. *Sol. Energy* 249, 183–226. <https://doi.org/10.1016/j.solener.2022.10.041>.

- [28] Khosa, A.A., Xu, T., Xia, B.Q., Yan, J., Zhao, C.Y., 2019. Technological challenges and industrial applications of CaCO₃/CaO based thermal energy storage system – A review. *Sol. Energy* 193, 618–636. <https://doi.org/10.1016/j.solener.2019.10.003>.
- [29] Lawn, B.R., Swain, M.V., 1975. Microfracture beneath point indentations in brittle solids. *J. Mater. Sci.* 10 (1), 113–122. <https://doi.org/10.1007/BF00541038>.
- [30] Li, B., Li, Y., Dou, Y., Wang, Y., Zhao, J., Wang, T., 2021. SiC/Mn co-doped CaO pellets with enhanced optical and thermal properties for calcium looping thermochemical heat storage. *Chem. Eng. J.* 423, 130305 <https://doi.org/10.1016/j.cej.2021.130305>.
- [31] Liu, F., Song, C., Zhu, D., Li, C., Ai, L., Xin, C., Zeng, X., Zeng, L., Huang, N., Yang, L., 2023. Attrition and attrition-resistance of oxygen carrier in chemical looping process – A comprehensive review. *Fuel* 333, 126304. <https://doi.org/10.1016/j.fuel.2022.126304>.
- [32] Mahroug, I., Doppiu, S., Dauvergne, J.-L., Palomo del Barrio, E., 2022. Li₄(OH) 3Br/MgO shape stabilized composite as novel high temperature thermal energy storage material. *J. Storage Mater.* 52, 104921 <https://doi.org/10.1016/j.est.2022.104921>.
- [33] Mohrbacher, H., Celis, J.P., Roos, J.R., 1995. Laboratory testing of displacement and load induced fretting. *Tribol. Int.* 28 (5), 269–278. [https://doi.org/10.1016/0301-679X\(95\)00005-0](https://doi.org/10.1016/0301-679X(95)00005-0).
- [34] Moya, J., Marugán, J., Orfila, M., Díaz-Pérez, M.A., Serrano-Ruiz, J.C., 2021. Improved thermochemical energy storage behavior of manganese oxide by molybdenum doping. *Molecules* 26 (3), 583.
- [35] Pardo, P., Deydier, A., Anxionnaz-Minvielle, Z., Rougé, S., Cabassud, M., Cognet, P., 2014. A review on high temperature thermochemical heat energy storage. *Renew. Sustain. Energy Rev.* 32, 591–610. <https://doi.org/10.1016/j.rser.2013.12.014>.
- [36] Peterson, S.B., Konya, G., Clayton, C.K., Lewis, R.J., Wilde, B.R., Eyring, E.M., Whitty, K.J., 2013. Characteristics and CLOU performance of a novel SiO₂-supported oxygen carrier prepared from CuO and β-SiC. *Energy Fuel* 27 (10), 6040–6047. <https://doi.org/10.1021/ef401365h>.
- [37] Ping, X., Jianjun, Z., Yunlong, A., Wen, H., Bingliang, L., Weihua, C., 2019. Vacuum sintering and performance of SiC doped WC-10Ni cemented carbide. *Rare Metal Mater. Eng.* 48 (2), 566–572.
- [38] Powell, M.S., Weerasekara, N.S., Cole, S., LaRoche, R.D., Favier, J., 2011. DEM modelling of liner evolution and its influence on grinding rate in ball mills. *Miner. Eng.* 24 (3), 341–351. <https://doi.org/10.1016/j.mineng.2010.12.012>.
- [39] Preisner, N.C., Block, T., Linder, M., Leion, H., 2018. Stabilizing particles of manganese-iron oxide with additives for thermochemical energy storage. *Energy Technol.* 6 (11), 2154–2165. <https://doi.org/10.1002/ente.201800211>.
- [40] Project, S., 2011. Thermochemical heat storage for concentrated solar power. United States.
- [41] Schrader, A.J., Schieber, G.L., Ambrosini, A., Loutzenhiser, P.G., 2020. Experimental demonstration of a 5 kWh granular-flow reactor for solar thermochemical energy storage with aluminum-doped calcium manganite particles. *Appl. Therm. Eng.* 173, 115257 <https://doi.org/10.1016/j.applthermaleng.2020.115257>.
- [42] Sunku Prasad, J., Muthukumar, P., Desai, F., Basu, D.N., Rahman, M.M., 2019. A critical review of high-temperature reversible thermochemical energy storage systems. *Appl. Energy* 254, 113733. <https://doi.org/10.1016/j.apenergy.2019.113733>.
- [43] Thommes, M., Kleinebudde, P., 2017. The science and practice of extrusion-spheronization. In: Rajabi-Siahboomi, A.R. (Ed.), *Multiparticulate Drug Delivery: Formulation, Processing and Manufacturing*. Springer, New York, New York, NY, pp. 37–63.
- [44] Wang, B., Wang, Z., Dou, B., Ma, Y., Liang, Y., 2021. Effects of TiO₂ doping on the performance of thermochemical energy storage based on Mn₂O₃/Mn₃O₄ redox materials. *RSC Adv.* 11 (53), 33744–33758. <https://doi.org/10.1039/D1RA05472D>.
- [45] Wang, N., Lu, H., Xu, J., Guo, X., Liu, H., 2019. Granular flows of binary mixtures down an inclined channel. *Int. J. Multiph. Flow* 120, 103097. <https://doi.org/10.1016/j.ijmultiphaseflow.2019.103097>.
- [46] Wokon, M., Block, T., Nicolai, S., Linder, M., Schmücker, M., 2017. Thermodynamic and kinetic investigation of a technical grade manganese-iron binary oxide for thermochemical energy storage. *Sol. Energy* 153, 471–485. <https://doi.org/10.1016/j.solener.2017.05.045>.
- [47] Wokon, M., Kohzer, A., Linder, M., 2017. Investigations on thermochemical energy storage based on technical grade manganese-iron oxide in a lab-scale packed bed reactor. *Sol. Energy* 153, 200–214. <https://doi.org/10.1016/j.solener.2017.05.034>.
- [48] Wong, B., Brown, L., Schaub, F., Tamme, R., Sattler, C., 2010. *Oxide Based Thermochemical Heat Storage*. SolarPACES, Perpignan, France.
- [49] Xiang, D., Gu, C., Xu, H., Xiao, G., 2021. Self-Assembled Structure Evolution of Mn Fe Oxides for High Temperature Thermochemical Energy Storage. *Small* 17 (29), 2101524. <https://doi.org/10.1002/sml.202101524>.
- [50] Xiao, G., Grace, J.R., Lim, C.J., 2011. Attrition characteristics and mechanisms for limestone particles in an air-jet apparatus. *Powder Technol.* 207 (1), 183–191. <https://doi.org/10.1016/j.powtec.2010.10.028>.
- [51] Yarrington, J.D., Bagepalli, M.V., Pathikonda, G., Schrader, A.J., Zhang, Z.M., Ranjan, D., Loutzenhiser, P.G., 2021. Numerical analyses of high temperature dense, granular flows coupled to high temperature flow property measurements for solar thermal energy storage. *Sol. Energy* 213, 350–360. <https://doi.org/10.1016/j.solener.2020.10.085>.
- [52] Yilmaz, D., Darwish, E., Leion, H., 2020. Investigation of the combined Mn-Si oxide system for thermochemical energy storage applications. *J. Storage Mater.* 28, 101180 <https://doi.org/10.1016/j.est.2019.101180>.